The Primordial Inflation Explorer (PIXIE)

Alan Kogut[a], Jens Chluba[b], Dale J. Fixsen[c], Stephan Meyer[d], and David Spergel[e]

[a]Code 665, NASA Goddard Space Flight Center, Greenbelt, MD USA 20771
[b]Jodrell Bank Centre for Astrophysics, University of Manchester, Oxford Road, Manchester M13 9PL, UK
[c]University of Maryland, College Park MD USA
[d]Dept of Astronomy & Astrophysics, University of Chicago, Chicago, IL, USA
[e]Dept of Astrophysical Sciences, Princeton University, Princeton, NJ, USA 08544

ABSTRACT

The Primordial Inflation Explorer is an Explorer-class mission to open new windows on the early universe through measurements of the polarization and absolute frequency spectrum of the cosmic microwave background. PIXIE will measure the gravitational-wave signature of primordial inflation through its distinctive imprint in linear polarization, and characterize the thermal history of the universe through precision measurements of distortions in the blackbody spectrum. PIXIE uses an innovative optical design to achieve background-limited sensitivity in 400 spectral channels spanning over 7 octaves in frequency from 30 GHz to 6 THz (1 cm to 50 micron wavelength). Multi-moded non-imaging optics feed a polarizing Fourier Transform Spectrometer to produce a set of interference fringes, proportional to the difference spectrum between orthogonal linear polarizations from the two input beams. Multiple levels of symmetry and signal modulation combine to reduce systematic errors to negligible levels. PIXIE will map the full sky in Stokes I, Q, and U parameters with angular resolution 2.6° and sensitivity 70 nK per 1° square pixel. The principal science goal is the detection and characterization of linear polarization from an inflationary epoch in the early universe, with tensor-to-scalar ratio $r < 10^{-3}$ at 5 standard deviations. The PIXIE mission complements anticipated ground-based polarization measurements such as CMB-S4, providing a cosmic-variance-limited determination of the large-scale E-mode signal to measure the optical depth, constrain models of reionization, and provide a firm detection of the neutrino mass (the last unknown parameter in the Standard Model of particle physics). In addition, PIXIE will measure the absolute frequency spectrum to characterize deviations from a blackbody with sensitivity 3 orders of magnitude beyond the seminal COBE/FIRAS limits. The sky cannot be black at this level; the expected results will constrain physical processes ranging from inflation to the nature of the first stars and the physical conditions within the interstellar medium of the Galaxy. We describe the PIXIE instrument and mission architecture required to measure the CMB to the limits imposed by astrophysical foregrounds.

Keywords: cosmic microwave background, polarimeter, spectral distortion, blackbody spectral distortions, Fourier transform spectrometer

1. INTRODUCTION

The cosmic microwave background (CMB) provides powerful tests for cosmology. A thermal remnant from the early universe, it dominates the sky at millimeter wavelengths and encodes information over the entire history of the universe. Its blackbody spectrum provides compelling evidence for a hot, dense phase at very early times, while the angular distribution of small temperature perturbations about the mean constrain the geometry and constituents of the universe. With only 6 free parameters, a single cosmological model successfully describes data sampling the universe over some 15 orders of magnitude in age, from the abundance of light elements shortly after the Big Bang to surveys of the locations and velocities of galaxies today. In this model, present-day structures form by gravitational infall and collapse seeded by a nearly scale-invariant power spectrum of Gaussian adiabatic initial density perturbations. The geometry of the universe is nearly flat, dominated by a cosmological constant Λ currently accelerating the expansion of the universe. The matter content is dominated by cold dark matter

---

Send correspondence to: Alan.J.Kogut@nasa.gov; telephone 001 301 286 0853

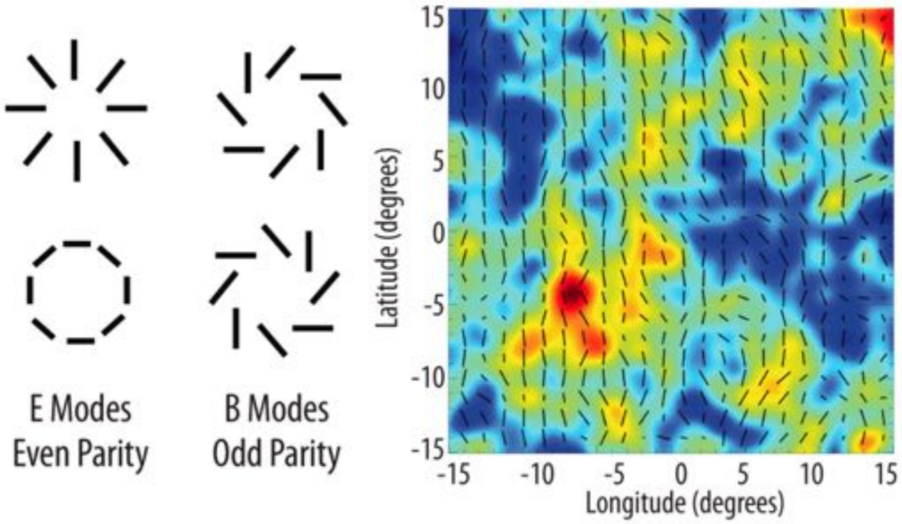

Figure 1. Simulated sky map showing CMB anisotropy (color) and polarization over a 30° × 30° patch of sky. The polarization pattern can be decomposed into even-parity E-modes and odd-parity B-modes. Only gravitational waves can produce a B-mode signal in the CMB on large angular scales.

currently observable only through its gravitational interactions; baryonic matter makes up only a few percent of the total density (see, e.g., 1).

Within this standard model, however, profound questions remain. The concordance ΛCDM model postulates that early in its history, the universe underwent a rapid period of superluminal expansion called inflation. Inflation provides an elegant explanation for the observed flatness and density fluctuations, but it relies on extrapolation of physics to energies greatly in excess of direct experimental data. Furthermore, not all constituents of the Universe in this model are well understood. Although high energy physics offers several attractive dark matter candidates, dark matter itself has never been directly observed.

New measurements of the CMB provide critical tests of the standard cosmological model. One such test is linear polarization. Gravitational waves created during an inflationary epoch interact with the CMB at much later times to create a distinctive signature in linear polarization. CMB polarization results from Thomson scattering of CMB photons by free electrons. Scattering of an isotropic radiation field produces no net polarization, but a quadrupole moment in the incident radiation yields a net polarized signal. There are two possible sources for such a quadrupole: an intrinsic temperature anisotropy or the differential redshift caused by gravitational waves. The two can be distinguished by their different spatial signatures (Figure 1). Temperature perturbations are scalar quantities; their polarization signal must therefore be curl-free. Gravitational waves, however, are tensor perturbations whose polarization includes both gradient and curl components. In analogy to electromagnetism, the scalar and curl components are often called "E" and "B" modes. Only gravitational waves induce a curl component: detection of a B-mode signal in the CMB polarization field is thus recognized as a "smoking gun" signature of inflation, testing physics at energies inaccessible through any other means.[2–9]

The amplitude of the gravitational wave signal depends on the value of the inflationary potential

$$V^{1/4} = 1.06 \times 10^{16} \text{ GeV} \left(\frac{r}{0.01}\right)^{1/4} \tag{1}$$

where r is the power ratio of gravitational waves to density fluctuations. If inflation results from Grand Unified Theory physics (energy $\sim 10^{16}$ GeV), the B-mode amplitude should be in the range 1 to 100 nK. Signals at this amplitude could be detected by a dedicated polarimeter, providing a critical test of a central component of modern cosmology. Detection of a gravitational-wave component in the CMB polarization would have profound implications for both cosmology and high-energy physics. It would establish inflation as a physical reality, provide a direct, model-independent determination of the relevant energy scale, and test physics at energies a trillion times beyond those accessible to particle accelerators. Generation of gravitational waves during inflation is purely a quantum-mechanical process: a detection of the B-mode signal provides direct observational evidence that gravity obeys quantum mechanics.

Distortions in the CMB blackbody spectrum provide a second powerful test for cosmology. Interactions between photons and charged particles at redshift $z > 2 \times 10^6$ rapidly establish thermal equilibrium, with the photon spectrum given by the familiar Planck formula

$$I(\nu, T) = \frac{2h\nu^3}{c^2} \frac{1}{\exp(h\nu/kT) - 1} \ , \tag{2}$$

where h is Planck's constant, k is Boltzmann's constant, c is the speed of light, ν is the frequency, and T is the photon temperature. Energy released at lower redshift heats the electron gas, which then distorts the CMB spectrum as the CMB photons Compton scatter to higher energies. Once photon-creating processes become negligible at redshift $z \lesssim 2 \times 10^6$, the spectrum is unable to evolve to a (hotter) blackbody, locking in a spectral distortion whose amplitude and spectral shape depend on the epoch, duration, and ratio of the energy released to that of the CMB photon bath.[10–14]

The Primordial Inflation Explorer (PIXIE) is an Explorer-class mission designed to measure both the inflationary signature in polarization and the blackbody spectral distortions from more recent cosmological epochs.[15] A "light bucket" optical design provides nK sensitivity using only four multi-moded detectors. A polarizing Fourier Transform Spectrometer synthesizes 400 channels across 7.5 octaves in frequency to provide unparalleled separation of CMB from Galactic foregrounds. PIXIE's highly symmetric design enables nulling operation to provide the necessary control of instrumental effects. The unique design achieves breakthrough sensitivity to both polarization and spectral distortions. We describe the PIXIE instrument and mission architecture and discuss how PIXIE can met the challenging science goals within the resources of the existing Explorer program.

2. SCIENCE GOALS

Recognizing the fundamental importance of precision CMB data, NASA's strategic planning specifically calls for new measurements of both CMB polarization and spectral distortions.

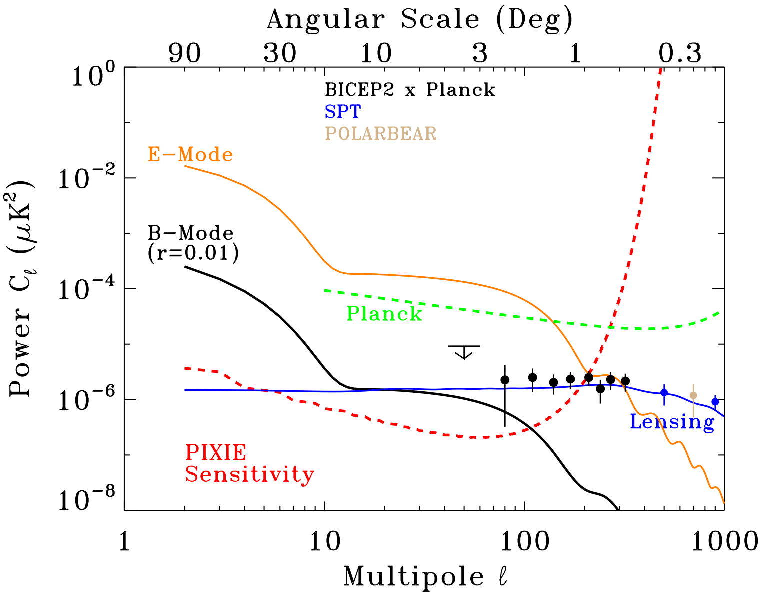

Figure 2. Angular power spectrum C_ℓ for CMB polarization. PIXIE can unambiguously detect the inflationary signal to 95% CL limit $r < 4 \times 10^{-4}$ while mapping the E-mode signal to the cosmic variance limit.

2.1 CMB Polarization

Measurements of unpolarized CMB fluctuations have tested a number of predictions of the simplest inflationary models: the universe is spatially flat with a background of scale-invariant, Gaussian, and adiabatic density perturbations. Measurements of CMB polarization tests the remaining prediction of inflation: the existence of gravitational waves generated during the inflationary expansion.

Figure 2 shows the angular power spectrum for polarization of the cosmic microwave background. Scalar (density) perturbations source E-mode polarization with amplitudes $\sim 1\ \mu$K on degree angular scales or larger. Gravitational lensing of the background E-mode pattern by the intervening mass distribution induces a small shear component, converting a fraction of the dominant E-mode signal to a B-mode pattern. Current measurements have begun to map the lensing signal while setting limits $r < 0.07$ to the inflationary signal.[16–18]

Large-field inflationary models suggest that a detectable B-mode signal should exist. The transition out of the inflationary epoch breaks pure scale invariance; the resulting signature in the density perturbations can be used to predict the accompanying signal in gravitational waves. The measured 5σ deviation from scale invariance[1] suggests a B-mode signal at the level $r > 0.01$. Signals at this level can be detected by a dedicated polarimeter, confirming a key prediction of inflation.

Full-sky measurements at nK sensitivity will also characterize the larger E-mode signal. The rise in E-mode power on angular scales greater than 20° (multipole $\ell < 10$) results from Thomson scattering during reionization and carries information on the ionization history of the universe. The optical depth τ to this scattering is partially degenerate with other cosmological parameters: an improved determination of τ improves constraints on other parameters. One example is the neutrino mass. Measurements of the lensing B-mode signal on arc-min angular scales constrain the sum Σm_ν of massive neutrino species. Figure 3 compares the limits on Σm_ν predicted for a combination of a redshift survey such as DESI with arcmin CMB polarization data from planned ground-based consortia such as CMB-S4. PIXIE will obtain a cosmic-variance-limited measurement of τ to detect the neutrino mass at 3 standard deviations, filling in the last unknown parameter in the Standard Model of particle physics.

2.2 Spectral Distortions

Measurements of the blackbody intensity spectrum provide a complementary window into the early universe. Figure 4 shows current measurements of the CMB intensity vs frequency. The CMB is well described by a

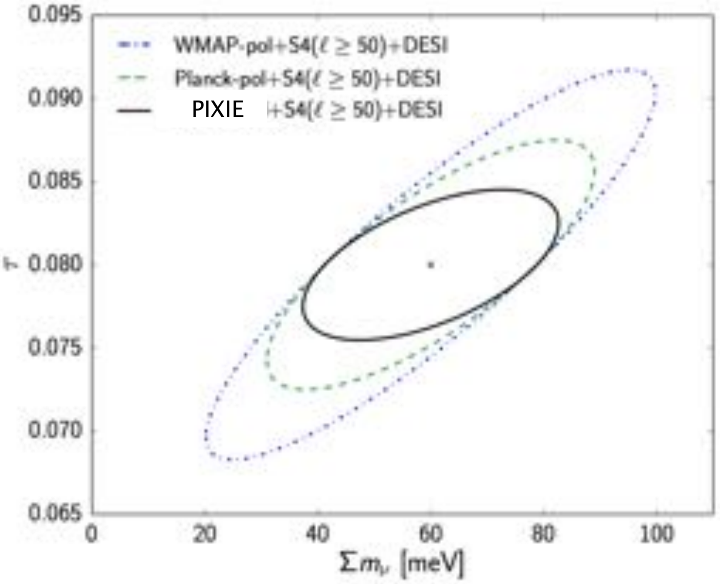

Figure 3. Predicted uncertainties for the summed neutrino mass vs optical depth τ from measurements of the E-mode polarization. PIXIE will measure τ to the cosmic-variance limit to provide a firm detection of the neutrino mass.

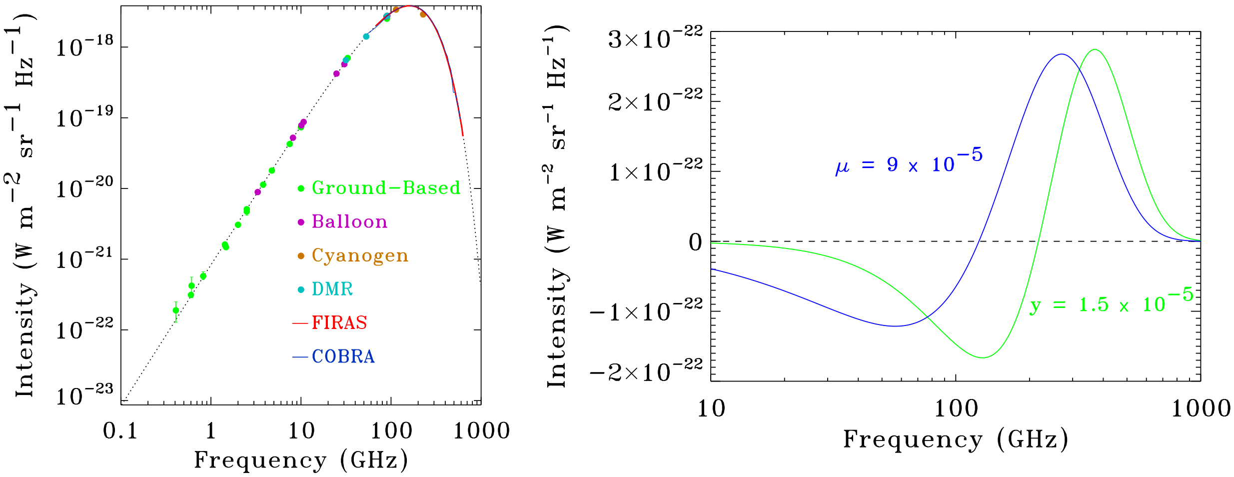

Figure 4. CMB intensity spectrum and spectral distortions. (Left) The absolute intensity of the CMB follows a blackbody Planck distribution. (Right) y and μ spectral distortions at the FIRAS 95% confidence upper limit.

Planckian spectrum over some 4 decades in frequency or intensity. The COBE/FIRAS and COBRA missions limit deviations from a Planck spectrum to $\Delta I/I < 50$ parts per million at millimeter wavelengths. Balloon and ground-based measurements at longer wavelengths have larger uncertainties but show no evidence for significant primordial distortions.

Spectral distortions result from the scattering of CMB photons by free electrons. Optically thin scattering at $z_r < 10^4$ generates a Compton distortion

$$\frac{\Delta I}{I} = y \frac{x e^x}{e^x - 1} \left[x \frac{e^x + 1}{e^x - 1} - 4 \right] \tag{3}$$

characterized by the parameter

$$y = \int \frac{k[T_e(z) - T(z)]}{m_e c^2} n_e(z) \sigma_T c \, dz, \tag{4}$$

where $x = h\nu/kT$, m_e, n_e, and T_e are the electron mass, number density, and temperature, and σ_T is the Thomson cross section.[10] For early energy releases $3 \times 10^5 < z_r < 2 \times 10^6$, multiple scatterings create statistical equilibrium, leading to a distorted spectrum

$$I(\nu, T) = \frac{2h\nu^3}{c^2} \frac{1}{\exp(h\nu/kT - \mu) - 1} \tag{5}$$

with chemical potential

$$\mu = 1.4 \, \frac{\Delta E}{E} \tag{6}$$

proportional to the fractional energy release relative to the CMB.[19,20] For intermediate redshifts $10^4 < z_r < 3 \times 10^5$ the spectrum is mixed.[14,21]

FIRAS limits spectral distortions to $|y| < 15 \times 10^{-6}$ and $|\mu| < 9 \times 10^{-5}$.[22] Figure 4 shows y-type and μ-type spectral distortions at these limits. Experimental design can improve the FIRAS limits by 3 orders of magnitude. The sky cannot be black at this level; a number of known astrophysical processes will create distortions at the 50 part-per-billion level. Consider, for instance, Compton scattering by thermal electrons within groups and clusters of galaxies, often called the Sunyaev-Zeldovich (SZ) effect. The Planck satellite has mapped the SZ effect from the brighter sources in the sky.[23] The integrated distortion from mapped clusters is $y > 5 \times 10^{-8}$.[24] Including the contribution from the expected population of unresolved fainter sources increases the distortion to $y \simeq 1.6 \times 10^{-6}$ only a factor of 10 below current upper limits.[25] PIXIE will detect this integrated y distortion at

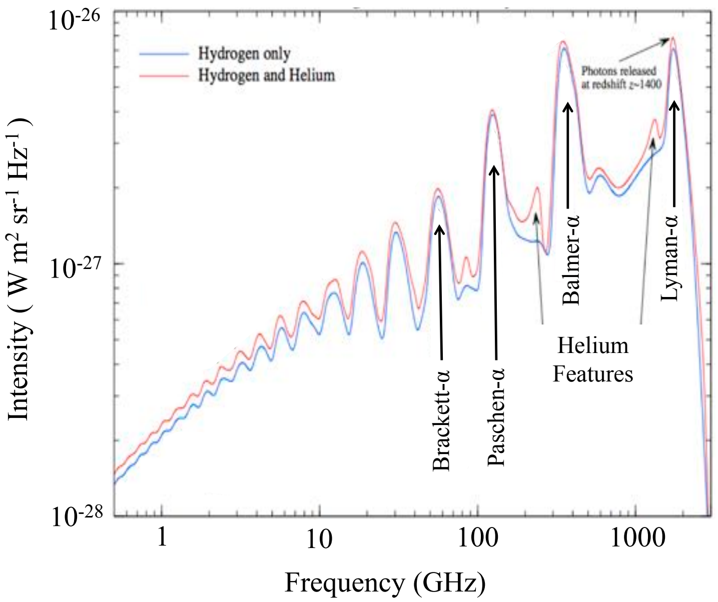

Figure 5. Spectral distortion from recombination (adapted from 29). PIXIE can achieve a statistical detection of the recombination distortion, testing physics at recombination.

over 1000 standard deviations, allowing a clear separation of relativistic from non-relativistic effects. The high signal-to-noise ratio further allows PIXIE to map spatial fluctuations in the y distortion; cross-correlation of the resulting SZ maps with maps of the galaxy distribution offers the exciting possibility of y-distortion tomography to trace the growth of structure and explore the role of feedback in galaxy evolution.

Other distortions must be present at potentially detectable levels. Silk damping of density perturbations on small physical scales transfers energy from the scalar perturbations to the average CMB spectrum, creating a chemical potential distortion $\mu \sim 2 \times 10^{-8}$.[26–29] The amplitude of the density perturbations on these small (solar mass) scales depends on the scalar power spectrum; measurements of the chemical potential constrain the spectral index n_s and running of the index to physical scales some 4 orders of magnitude beyond those probed by the damping tail of the unpolarized CMB power spectrum.

Recombination of hydrogen and helium at $z \sim 1000$ provide a rich series of lines distorting the smooth Planck function (Figure 5. A detection of these lines tests physics at recombination and constrains the primordial helium abundance well before contamination by stellar processes.[29] A statistical detection of these lines requires sensitivity $\delta I/I \sim 10^{-6}$ and spectral resolution of a few to perhaps 50 GHz. Using the recombination ”fingerprint” as a template, the baseline PIXIE mission would provide a statistical detection of these lines at 2–4 standard deviations.

Decay or annihilation of dark matter provides another source of energy injection into the early universe. For Majorana particles, the annihilation rate varies as the density n^2, while the density varies as redshift z^3. Annihilation is thus most effective at high redshift, leading to a μ-type distortion

$$m_\chi > 80\text{keV} \left[f \left(\frac{\mu}{5 \times 10^{-8}} \right) \left(\frac{\sigma v}{6 \times 10^{-27} \text{cm}^3 \text{s}^{-1}} \right) \left(\frac{\Omega_\chi}{0.112} \right)^2 \right]^{1/2}, \tag{7}$$

where f is the fraction of annihilation products into charged particles.[30] Since the number density varies inversely with the particle mass, limits to μ distortions can constrain the mass m_χ and cross-section σv of light dark matter candidates such as sterile neutrinos, complementing gamma-ray limits to heavy (GeV) dark-matter candidates.

2.3 PIXIE Mission

Compelling scientific results await a new generation of CMB measurements. Such a measurement will be challenging, requiring characterization of primordial signals at the ten parts-per-billion level in the presence of much brighter foregrounds from both local and cosmological sources. Several principles guide the mission design.

- **Null Detection** The mission design should minimize offsets, responding only to the signal of interest while producing zero instantaneous response to unwanted sources. Signal differencing should be performed pre-detection to avoid dependence on instrument calibration.
- **Modulation** The mission design should include multiple levels of signal modulation to separate sky signals from instrumental effects.
- **Symmetry** The mission design should include multiple symmetries to cross-check the results. Comparison of sum and difference 'jack-knife" tests enables identification and subtraction of residual instrumental effects.

PIXIE uses an innovative optical design to achieve these goals in a compact configuration. A cryogenic "light bucket" maintained within a few mK of the CMB temperature forms a blackbody cavity to minimize instrumental offsets, reducing the instrumental signature by a factor of 300 compared to 4 K optics. A nulling Fourier transform spectrometer (FTS) interferes two co-pointed beams to measure either the difference in orthogonal polarization states between the beams or the spectral distortion between the sky and an on-board blackbody cavity. Null operation reduces dependence on calibration stability by nearly six orders of magnitude. The optical phase delay in the FTS and the spacecraft spin combine to produce a complex amplitude modulation for any true sky signal. Some twenty discrete symmetries provide a rich set of jack-knife tests, each of which uses the full data set. All

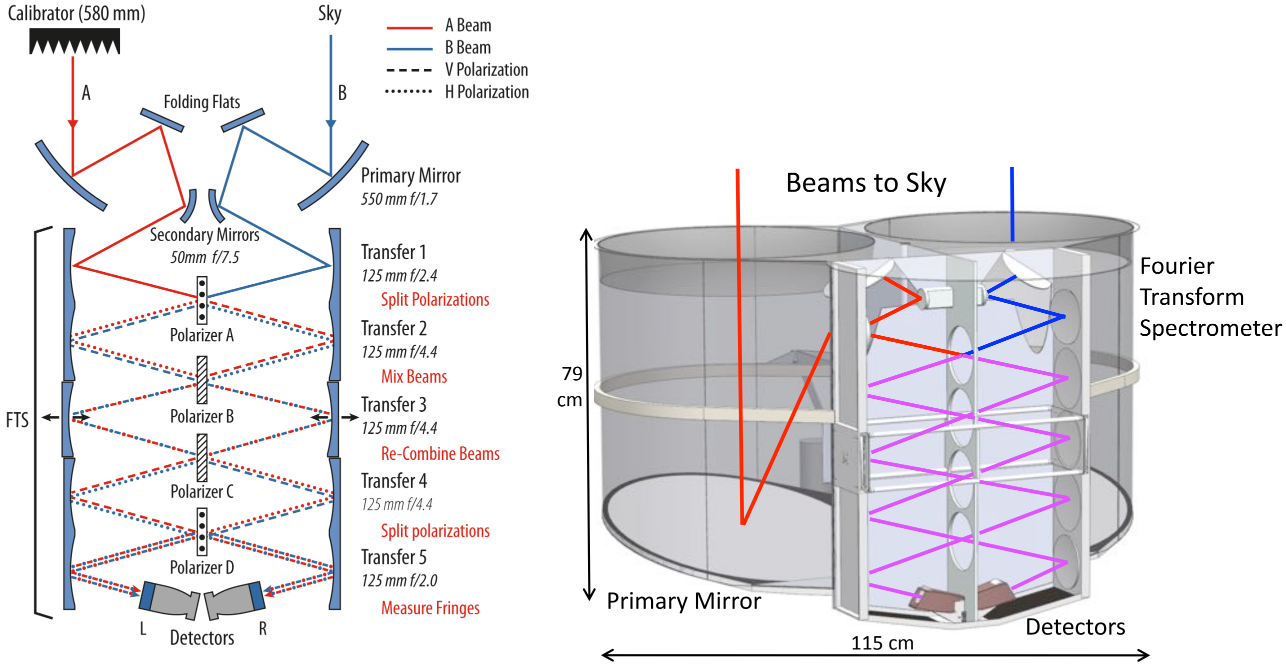

Figure 6. (Left) Schematic view of the PIXIE optical signal path. A polarizing Fourier transform spectrometer interferes the signal from two co-pointed beams to produce a fringe pattern proportional to the difference spectrum between orthogonal polarization states from the two beams (Stokes Q in instrument coordinates). A full-aperture blackbody calibrator can move to block either input beam, providing a null reference for spectral distortions. The entire instrument in maintained within 5 mK of the CMB, reducing potential instrumental effects. (Right) Physical layout of PIXIE optics.

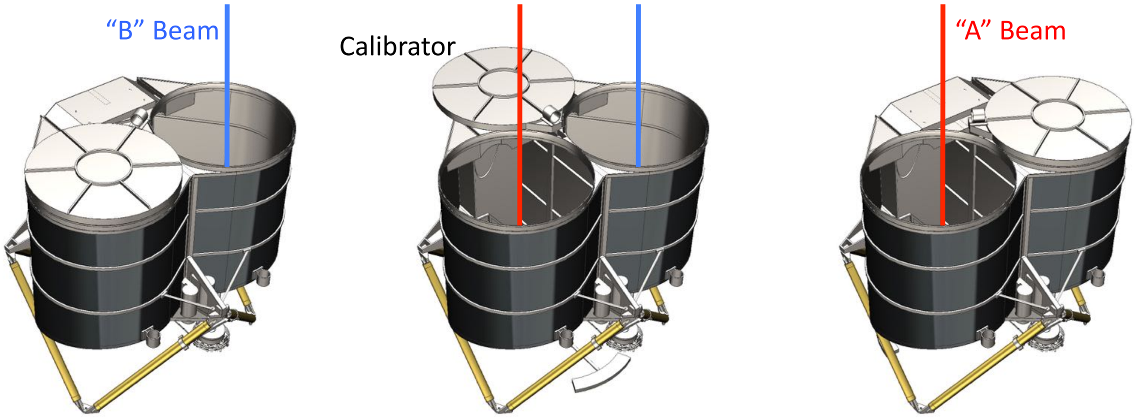

Figure 7. An external blackbody calibrator can be commanded to one of three positions: completely blocking the "A" beam (left panel), completely blocking the "B" beam (right panel), or stowed so that both beams view the sky (center). With the calibrator stowed, PIXIE operates as a nulling polarimeter insensitive to unpolarized emission. With the calibrator deployed over either beam, PIXIE is sensitive to both polarization and spectral distortions relative to the blackbody calibrator.

optical frequencies are incident on each detector at all times, greatly simplifying calibration: Fourier transform of the observed fringe pattern yields a null measurement with high sensitivity in 400 frequency channels across 7 octaves in frequency.

2.4 Instrument Description

Figure 6 shows the instrument concept. Two off-axis primary mirrors 550 mm in diameter produce twin beams co-aligned with the spacecraft spin axis. A folding flat and 50 mm secondary mirror route the beams to the FTS. A set of five transfer mirror pairs, each imaging the previous mirror to the following one, shuttles the radiation through a series of polarizing wire grids. Polarizer A transmits vertical polarization and reflects horizontal polarization, separating each beam into orthogonal polarization states. A second polarizer (B) with wires oriented 45° relative to grid A mixes the polarization states. A Mirror Transport Mechanism (MTM) moves the central pair of transfer mirrors to inject an optical phase delay. The phase-delayed beams re-combine (interfere) at Polarizer C. Polarizer D (oriented the same as A) splits the beams again and routes them to two multi-moded concentrator feed horns. Each concentrator is square to preserve linear polarization[31] and contains a pair of identical bolometers, each sensitive to a single linear polarization but mounted at 90° to each other to measure orthogonal polarization states. To control stray light, all internal surfaces except the active optical elements are coated with a microwave absorber,[32] forming a blackbody cavity isothermal with the sky.

Each of the four detectors measures an interference fringe pattern between orthogonal linear polarizations from the two input beams. Let $\vec{E} = E_x \hat{x} + E_y \hat{y}$ represent the electric field incident from the sky. The power at the detectors as a function of the mirror position z may be written

$$\begin{aligned}
P_{Lx} &= 1/2 \int (E_{Ax}^2 + E_{By}^2) + (E_{Ax}^2 - E_{By}^2) \cos(4z\omega/c) d\omega \\
P_{Ly} &= 1/2 \int (E_{Ay}^2 + E_{Bx}^2) + (E_{Ay}^2 - E_{Bx}^2) \cos(4z\omega/c) d\omega \\
P_{Rx} &= 1/2 \int (E_{Ay}^2 + E_{Bx}^2) + (E_{Bx}^2 - E_{Ay}^2) \cos(4z\omega/c) d\omega \\
P_{Ry} &= 1/2 \int (E_{Ax}^2 + E_{By}^2) + (E_{By}^2 - E_{Ax}^2) \cos(4z\omega/c) d\omega \ , \qquad (8)
\end{aligned}$$

where L and R refer to the detectors in the left and right concentrators while A and B refer to the two input beams (Fig 6).

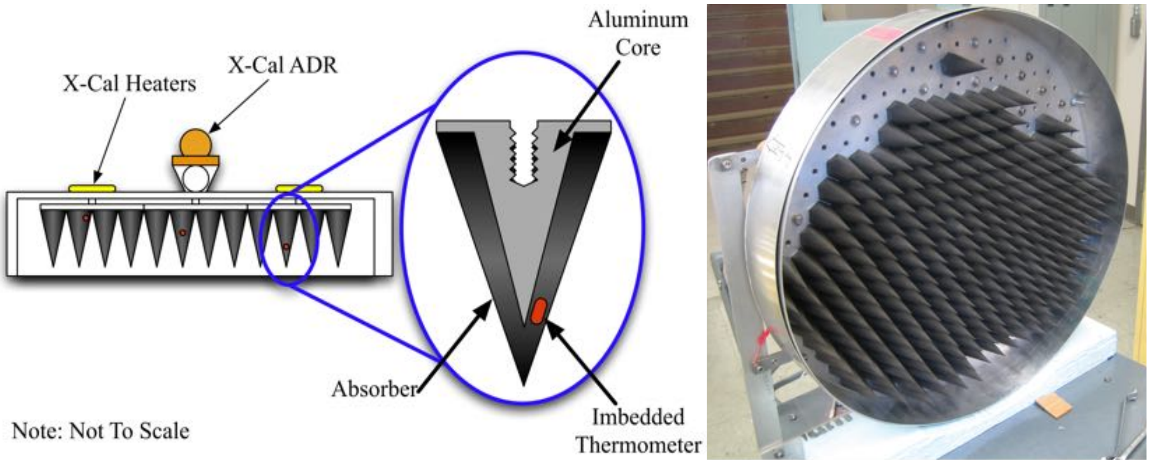

Figure 8. PIXIE calibrator design. (Left) The calibrator consists of a forest of absorbing cones mounted on a thermally conductive base. Thermometers embedded within selected cones monitor both the absolute temperature and temperature gradients. An adiabatic demagnetization refrigerator stores energy for thermal control. (Right) Photograph of the ARCADE calibrator during assembly. PIXIE uses a similar design with smaller cones to operate at shorter wavelengths.

The modulated term is proportional to Fourier transform of the frequency spectrum for Stokes Q linear polarization in instrument-fixed coordinates. Rotation of the instrument about the beam axis interchanges $\hat{x}$ and $\hat{y}$ on the detectors. The sky signal then becomes

$$\begin{aligned}
S(\nu)_{Lx} &= 1/4\,[\ I(\nu)_A - I(\nu)_B + Q(\nu)_{\rm sky}\cos 2\gamma + U(\nu)_{\rm sky}\sin 2\gamma\ ] \\
S(\nu)_{Ly} &= 1/4\,[\ I(\nu)_A - I(\nu)_B - Q(\nu)_{\rm sky}\cos 2\gamma - U(\nu)_{\rm sky}\sin 2\gamma\ ] \\
S(\nu)_{Rx} &= 1/4\,[\ I(\nu)_B - I(\nu)_A + Q(\nu)_{\rm sky}\cos 2\gamma + U(\nu)_{\rm sky}\sin 2\gamma\ ] \\
S(\nu)_{Ly} &= 1/4\,[\ I(\nu)_B - I(\nu)_A - Q(\nu)_{\rm sky}\cos 2\gamma - U(\nu)_{\rm sky}\sin 2\gamma\ ]\ ,
\end{aligned} \tag{9}$$

where $I = \langle E_x^2 + E_y^2 \rangle$, $Q = \langle E_x^2 - E_y^2 \rangle$, and $U = 2{\rm Re}\langle E_x E_y \rangle$ are the Stokes polarization parameters, γ is the spin angle, and $S(\nu)$ denotes the synthesized frequency spectrum with bins ν set by the fringe sampling.

PIXIE carries an on-board blackbody calibrator to provide an absolute reference signal The calibrator can be deployed to fully cover either one of the beams, or stowed so that both beams view the sky (Figure 7). When both beams view the sky, the instrument responds only to polarization, with the fringe pattern encoding the frequency spectrum of the polarized sky emission. When the calibrator blocks one of the beams, the fringe pattern encodes information for both polarization and the absolute intensity of the sky emission (Eq. 9).

Figure 8 shows the calibrator design. Based on the proven ARCADE design,[33] the PIXIE calibrator consists of 1369 absorbing cones, each 34 mm tall and 16 mm wide at the base, mounted in a close packed array on a thermally conductive aluminum plate 580 mm in diameter to fully cover one beam aperture. Each cone consists of a thermally conductive aluminum core covered with a thin absorptive skin,[32] with power reflection < -65 dB. Cernox thermometers in 39 selected cones monitor the temperature. The thermometers are cast into the absorber and calibrated *in situ* against absolute temperature standards from the National Institute for Standards and Technology. The calibrator temperature can be commanded within the range 2.6–3.5 K to provide a calibration signal at frequencies below 1 THz. Calibration at frequencies above the 600 GHz CMB Wien cutoff uses a single cone heated to 20 K. The fill factor (1/1369) and temperature are chosen to approximate the spectrum of the diffuse Galactic dust cirrus.

2.5 Cryogenic Design

Figure 9 shows the cryogenic design. A combination of passive and active cooling maintains the PIXIE instrument at cryogenic temperatures. A composite hexapod structure provides mechanical support and thermal isolation for the instrument. Nested thermal shields provide passive cooling at 150 K while shielding the instrument against

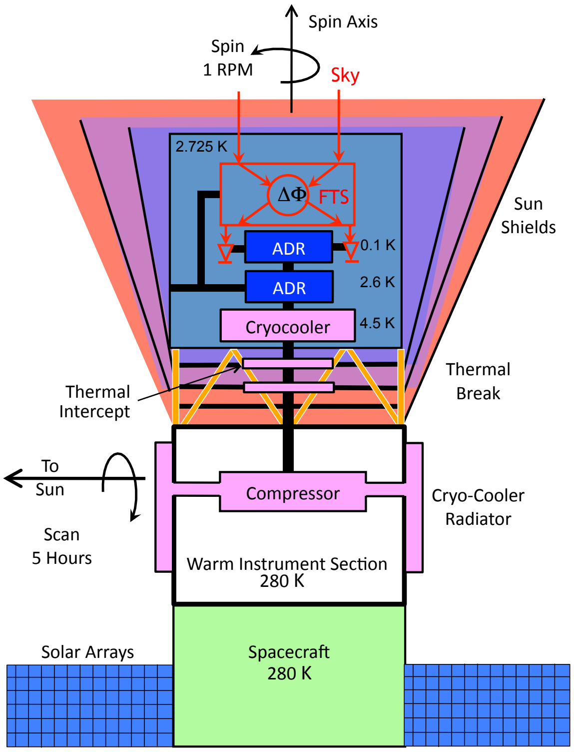

Figure 9. Cryogenic layout for the PIXIE instrument. An ADR and mechanical cryo-cooler maintain the instrument and enclosure at 2.725 K, isothermal with the CMB. A set of concentric shields surrounds the instrument to prevent heating by the Sun or spacecraft.

thermal emission from the Sun and warm spacecraft. A mechanical cryocooler provides cooling from 280 K to 4.5 K, with intermediate stages intercepting heat from the hexapod supports at 68 and 17 K. The cryocooler rejects heat to a dedicated radiator. Two adiabatic demagnetization refrigerator (ADR) systems based on the Hitomi mission cool the instrument and detectors. An instrument ADR provides a 2.6 K "thermal bus" to regulate the instrument at 2.725 K, while a second ADR provides 100 mK cooling for the detectors. The precise bus temperature is not critical; each instrument component (optics barrels, mirrors, polarizers, etc) is weakly connected to the bus to provide independent thermal control at 2.725 K. There are no stored cryogens, allowing operational resiliency.

2.6 Observatory and Mission Design

Figure 10 shows the observatory and mission concept. PIXIE will be placed in a large-amplitude halo orbit about the second Sun-Earth Lagrange point (L2). The instrument spins at approximately 1 RPM with the spin axis maintained 91° from the Sun line. The spin axis rotates about the sun line once every 5 hours to scan a circle on the sky. The pointing continuously follows the sun line throughout the year, so that the full sky is observed every six months. The detector sampling, mirror stroke, and spacecraft spin are fast compared to the scan motion of the beam across the sky, eliminating the need for pixel-to-pixel differences in the data analysis.

3. INSTRUMENT PERFORMANCE

PIXIE's optical design combines multi-moded optics with a Fourier Transform Spectrometer (FTS) to provide breakthrough sensitivity for precision CMB measurements. A multi-moded "light bucket" provides nK sensitivity using only four detectors. A polarizing Fourier Transform Spectrometer synthesizes 400 channels across 2.5 decades in frequency to provide unparalleled separation of CMB from Galactic foregrounds. PIXIE's highly symmetric design enables operation as a fully nulled instrument to provide the necessary control of instrumental effects.

3.1 Sensitivity

PIXIE uses muti-moded optics to achieve background-limited sensitivity with only 4 detectors. The noise equivalent power (NEP) of photon noise in a single linear polarization is given by

$$\mathrm{NEP}^2_{\mathrm{photon}} = \frac{2A\Omega}{c^2} \frac{(kT)^5}{h^3} \int \alpha \epsilon f \ \frac{x^4}{e^x - 1} \ \left(1 + \frac{\alpha \epsilon f}{e^x - 1}\right) \ dx, \tag{10}$$

where A is the detector area, Ω is the detector solid angle, α is detector absorptivity, T is the physical temperature of the source, ϵ is the emissivity of the source, and f is the power transmission through the optics.[34] For a fixed integration time τ the detected noise is simply

$$\delta P = \frac{\mathrm{NEP}}{\sqrt{\tau/2}} \tag{11}$$

where the factor of 2 accounts for the conversion between the frequency and time domains. The noise at the detector may in turn be referred to the specific intensity on the sky,

$$\delta I_\nu = \frac{\delta P}{A\Omega \ \Delta\nu \ (\alpha \epsilon f)} \tag{12}$$

where $\Delta\nu$ is the observing bandwidth.

PIXIE combines a large collecting area with non-imaging optics to maximize the number of photons while minimizing the detector count. The light-gathering ability of an instrument is specified by its etendu $A\Omega$. Increasing the etendu for a single detector increases the photon noise, NEP $\propto$ $(A\Omega)^{1/2}$. But since the signal increases linearly with etendu, the signal-to-noise ratio *improves* as $(A\Omega)^{1/2}$.

The multi-moded PIXIE optics provide sensitivity comparable to kilo-pixel focal plane arrays while requiring only 4 semiconductor bolometers. For diffraction-limited single-mode optics, the etendu and wavelength are

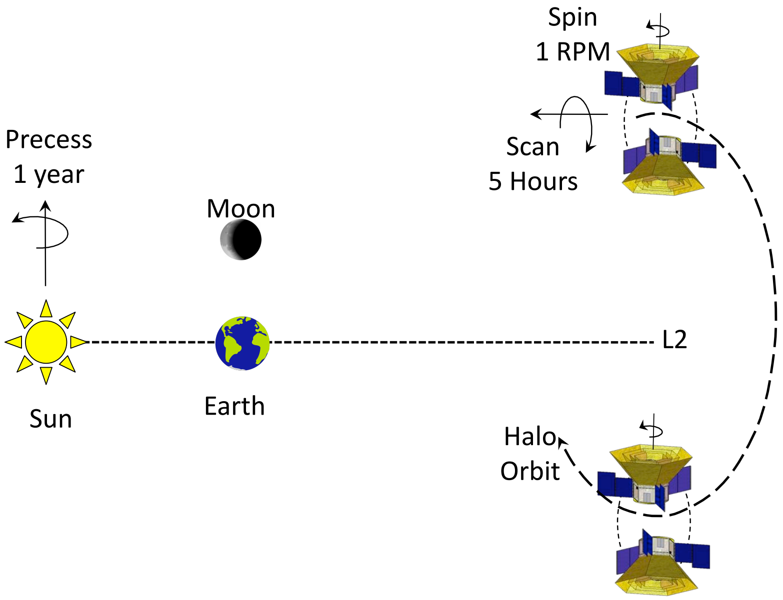

Figure 10. PIXIE observes from the Sun-Earth L2 point. The spin is fast compared to the great-circle scan so that every pixel on the sky has uniform coverage vs spin angle. The rapid spin and interferometer stroke efficiently separate Stokes I, Q, and U parameters independently within each pixel to provide a nearly diagonal covariance matrix.

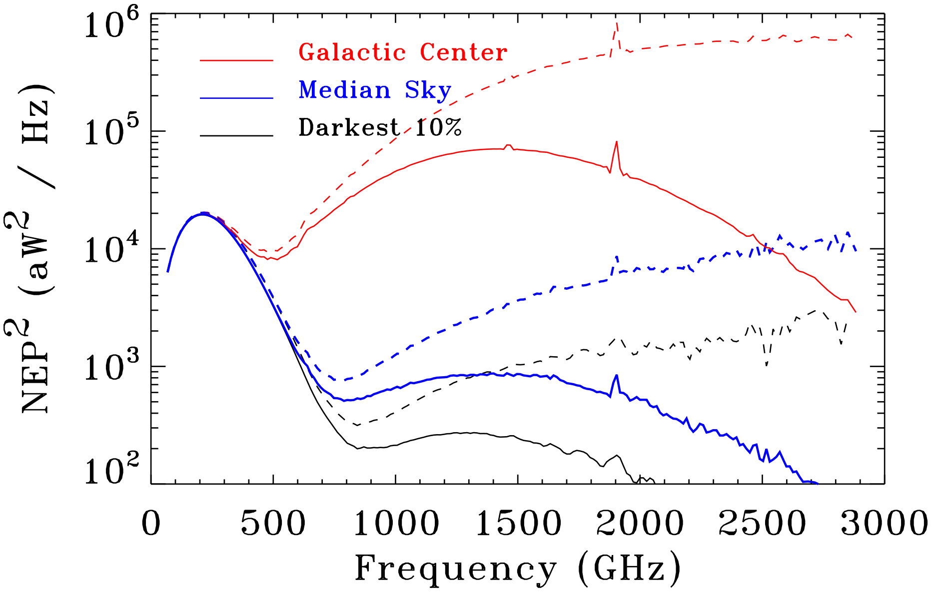

Figure 11. Photon noise from different parts of the sky. We include the contributions from the CMB, Galactic dust, zodiacal dust, and the far-IR background. The solid lie shows the differential NEP using the PIXIE low-pass filter while the dashed lines sow the NEP if no filter is applied (see text). A lowpass filter with knee frequency at 1.5 THz allows observation of the bright dust signal with only a modest increase to the photon noise budget.

related as $A\Omega = \lambda^2$ so that the beam size scales with the observing wavelength. For multi-moded optics, however, the beam size is fixed and the number of modes N scales as $N = A\Omega/\lambda^2$. Multi moded optics thus allow a considerable increase in sensitivity compared to single-moded designs of comparable size. The improvement is large enough to allow precision measurement of the gravitational-wave signature in polarization using a handful of detectors. Over just the frequency range 30–600 GHz where the CMB is brightest, each PIXIE detector measures 22,000 independent modes of the electric field.

The photon noise depends on the sky intensity. The FTS is intrinsically broadband: high-frequency photons above the Wien cutoff of the CMB spectrum can inject noise onto the detector and affect all channels of the synthesized spectra. We estimate this effect using Eq. 10 including contributions from the CMB, Galactic dust, the far-IR background, and Solar System zodiacal emission. Figure 11 shows the differential contribution to the NEP as a function of frequency (the integrand of Eq. 10) for three different regions of the sky: the Galactic center, the median sky, and the darkest 10%. At frequencies below 600 GHz, the photon noise budget is dominated by the CMB, while warmer sources contribute at higher frequencies. We limit the contribution from these sources using a low-pass filter to the optical system. A scattering filter on the folding flat with knee frequency ~1.5 THz rolls off the instrument response at higher frequencies, preferentially scattering short-wavelength emission out of the beam and onto the FTS walls where it is absorbed. This allows observation of the dust at THz frequencies surrounding the peak dust intensity while not significantly increasing the photon noise beyond the contribution from the CMB itself. Figure 12 shows the integrated photon noise after including the lowpass filter. We integrate Eq. 10 from 30 GHz to some maximum frequency, and show the resulting NEP as a function of the maximum observed frequency. With the lowpass filter in place, the penalty for FTS observations above 600 GHz is less than 20% of the CMB photon noise.

With the calibrator deployed over either aperture, the instrument measures both polarized and unpolarized emission (Stokes I, Q, and U). With both beams open to the sky, the instrument is insensitive to unpolarized emission but has twice the sensitivity to polarized signals[*]. Averaging over the four detectors, the combined

---

[*] Replacing the blackbody calibrator emission with sky emission in one beam leaves the noise nearly unchanged but doubles the sky signal incident on the FTS.

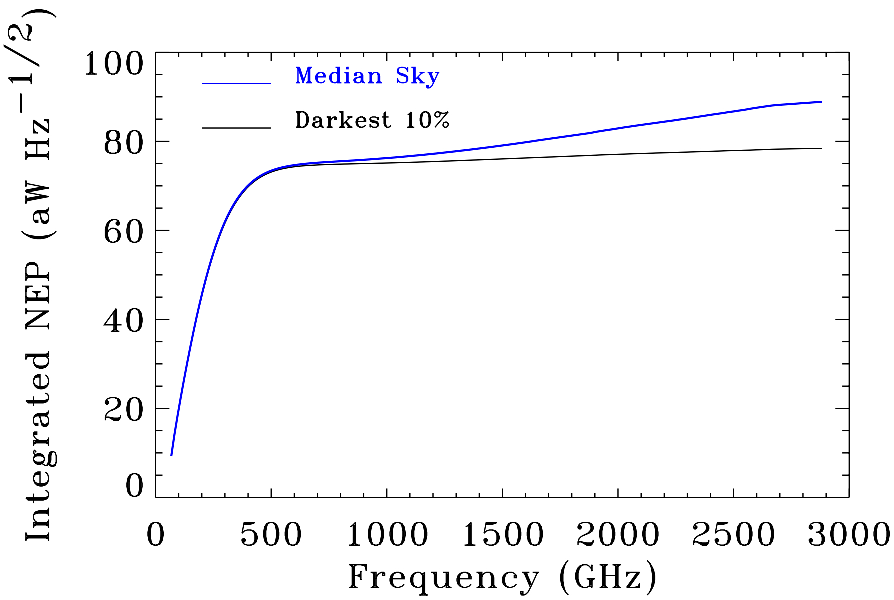

Figure 12. Photon noise contribution (Eq. 10) integrated over frequency, as a function of maximum observed frequency. Photon noise from dust and the far-IR background increases the noise less than 20% above the CMB photon noise.

instrument sensitivity to either unpolarized or polarized emission within each synthesized frequency bin is

$$\begin{aligned}\delta I_\nu^I &= 2.4 \times 10^{-22}\ \mathrm{W\ m^{-2}\ sr^{-1}\ Hz^{-1}} \\ \delta I_\nu^{QU} &= 3.4 \times 10^{-22}\ \mathrm{W\ m^{-2}\ sr^{-1}\ Hz^{-1}}\end{aligned} \quad (13)$$

for a one-second integration with the calibrator deployed over either aperture, and

$$\delta I_\nu^{QU} = 0.5 \times 10^{-22}\ \mathrm{W\ m^{-2}\ sr^{-1}\ Hz^{-1}} \quad (14)$$

when the calibrator is stowed.[15] PIXIE will spend approximately 45% of the observing time with the calibrator deployed over either beam, and 50% with the calibrator stowed. The remaining 5% includes both high-temperature calibration of the Galactic dust signal and lost observing time.

3.2 Frequency Channels

The fringe pattern measured at each detector samples the Fourier transform of the frequency spectrum of the difference between one linear polarization from the A-side beam and the orthogonal linear polarization from the B-side beam (Eq. 8). The frequency bins in the synthesized spectra $S(\nu)$ are set by the mirror throw and detector sampling,

$$S_\nu = \sum_{k=0}^{N_s-1} S_i \exp(2\pi i \nu k / N_s) \quad (15)$$

where S_i is a time-ordered sample and ν denotes frequency. As the mirror moves, we obtain N_s detector samples over an optical path length $\pm\Delta L$. The Fourier transform of the sampled fringe pattern returns frequencies $n\ \times c/(2\Delta L)$ where $n = 0, 1, 2, ..., N_s/2$. The path length (optical stroke) thus determines the width of the frequency bins in the synthesized spectra, while the number of detector samples within each optical stroke determines the number of frequency bins and thus the highest sampled frequency. For nominal operation we plan $N_s = 1024$ and $\Delta L = 1.04$ cm, to obtain 512 synthesized frequency bins of width 14.81 GHz each. The corresponding physical mirror movement $\Delta z = \Delta L/[4\cos(\alpha)\cos(\delta/2)] = \pm 2.7$ mm accounts for the folded optics as well as the off-axis optical path ($\alpha = 15°$) and beam divergence within the FTS ($\delta = 6.5°$).

PIXIE's Fourier transform spectroscopy provides a major advantage observing astrophysical sources such as the CMB and diffuse foregrounds. The bandpass for each synthesized channel is determined solely by the sampling of the interference fringe pattern and does not require separate bandpass measurements for each synthesized channel. Channel-to-channel cross-talk is also determined solely by the sampling, and can be limited using an appropriate choice of the apodization. We apodize the nominal Fourier transform by changing the mirror stroke during observations so that most strokes contain data near zero optical phase delay while relatively few strokes occur at large phase delay.

The nominal mirror stroke, and hence the synthesized channel width, is chosen to match the CO line emission ladder. The CO J=1–0 line at 115.3 GHz falls in the center of the 8th PIXIE channel, the J=2–1 line at 130.6 GHz falls in the center of the 16th PIXIE channel, and so forth. CO line emission is thus readily separable from continuum sources. Note that other analyses are possible. Line emission will typically have a width much less than the PIXIE synthesized channel width, diluting its amplitude within a single synthesized channel. Since line emission at a single frequency ν_0 creates a sinusoidal response at the appropriate spatial frequency in the interference fringe pattern, we may directly fit the observed fringe patterns for the response at spatial frequencies corresponding to far-IR emission lines (CII 158 μm, NII 122 and 205 μm, etc) to map these lines without dilution within the broader synthesized channels.

3.3 Systematic Errors

Measurements at the part-per-billion level require careful control of potential systematic errors. PIXIE uses a combination of null operation, signal modulation, and multiple discrete symmetries to reduce instrumental artifacts to negligible levels.

The first line of defense is null operation. The entire optical system, including all mirrors, polarizing grids, optical baffles, and walls, is maintained at temperatures $T_{\rm inst} = 2.725$ K, isothermal with the CMB. The instrument thus approximates a blackbody cavity: the largest possible contribution from *any* absorption or emission within the instrument itself cannot be larger than the few-mK difference between the instrument and the sky[†]. The FTS employs a second null, generating an interference fringe pattern proportional to the signal difference between two matched beams. With the calibrator stowed, the polarization signal depends on the difference between the horizontal polarization in one beam vs vertical polarization in the other, while with the calibrator deployed, the spectral signal depends on the difference between the sky and the blackbody calibrator.

Multiple symmetries combine with the double-null operation to reduce systematic effects to negligible levels. Consider, for instance, the effect of absorption from the primary mirror. Absorption at the primary mirror reduces the sky signal by an amount $\alpha I_{\rm sky}$ while adding emission $\alpha B_\nu(T_m)$ where $B_\nu(T)$ is the Planck function and T_m is the mirror temperature. Approximating the sky as a blackbody at $T_{\rm CMB} = 2.725$ K, emission from a single mirror creates an error signal

$$\Delta I = \alpha \left[B_\nu(T_m) - B_\nu(T_{\rm CMB}) \right] . \tag{16}$$

For $\alpha \sim 0.01$ typical for clean aluminum, the error for a single mirror is of order 0.01 × few mK, or a few tens of μK. Note that isothermal operation alone reduces this term by a factor of 300 or more compared to similar optical systems at temperatures $T_m \sim 4$K. The actual error is even smaller: the FTS differences the error signal generated by the A-side primary mirror against a similar signal from the B-side mirror. The differential error thus depends on the differential absorption $\Delta\alpha$ between the two mirrors,

$$\begin{aligned} \Delta I &= \Delta\alpha \left[B_\nu(T_m) - B_\nu(T_{\rm CMB}) \right] \\ &= \Delta\alpha \, \frac{\partial B_\nu}{\partial T} \, \Delta T \; , \end{aligned} \tag{17}$$

and not on the absolute absorption of either mirror. Assuming that the mirror absorption is matched to a few percent, the resulting systematic error is reduced by a corresponding amount, to levels of a few hundred nK.

[†] The CMB dipole causes the CMB temperature to vary by ±3 mK across the sky. We do not attempt to vary the instrument temperature to match the dipole as the instrument scans across the sky, but can use knowledge of the instrument–sky temperature difference to further identify and subtract instrumental effects. See below.

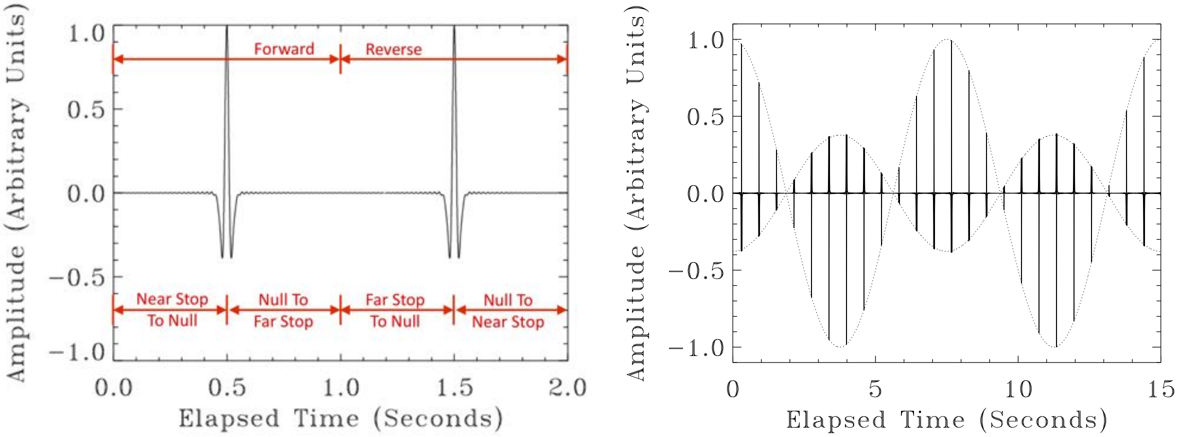

Figure 13. (Left) Simulated fringe pattern from a single detector observing a CMB source as the mirror scans through a complete cycle. Sky signals must follow multiple space- and time-reversal symmetries, allowing straightforward subtraction of instrumental signals. (Right) Fringe pattern from a polarized source for one complete spin period (shown here with mirror period 0.6 sec and spin period 15 sec). Sky rotation imposes an amplitude modulation on the entire fringe pattern to distinguish sky polarization from instrumental effects.

Signals at the hundred-nK-level are still large compared to the instrument sensitivity. We further reduce systematic effects by noting that the error signal depends on the temperature difference between the mirrors and the sky. If nothing else were done, observations of the hot and cold lobe of the CMB dipole would alternately make the sky hotter and colder than the mirror. To the extent that equal time is spent with the sky hotter than the mirror as colder than the mirror, the error signal will cancel, adding to the variance observed within any sky pixel but not contributing to the mean. This equality can always be enforced by an appropriate choice of weighting when mapping the time-ordered data to pixelized sky maps. Assuming that other constraints limit such weighting to few-percent precision, the remaining error signal is now reduced from a few hundred nK to a few nK.

In practice, each mirror has independent temperature control. The temperature of each mirror is intentionally varied by a few mK throughout the flight. By fitting the time-ordered data throughout the flight to the sky–mirror temperature difference (Eq. 17), we may directly measure the different absorption coefficients for each optical element and subtract the corresponding error signal prior to mapping. Since the error signal is fit using the *entire* time-ordered data set, the uncertainty in the resulting correction will be at the sub-nK precision of the full mission data set. Note that PIXIE's systematic error reduction does not rely on any single part-per-billion cancellation, but rather on a chain of percent-level cancellations operating multiplicatively.

Signal modulation further limits potential systematic errors. PIXIE employs at least three levels of modulation. The semiconductor detectors are ac-biased at approximately 1 kHz, limiting the effect of $1/f$ noise in the detector electronics. The mirror stroke transforms the spectro-polarimetric sky signal to a complex fringe pattern (Figure 13). Residual drifts or $1/f$ noise in the time domain, which typically induce map striping in conventional imaging instruments, are Fourier transformed into the frequency domain. They thus affect only the lowest few bins of the synthesized spectra in each sky pixel, and do not project onto continuum sources such as the CMB to cause striping in the maps.

The fringe pattern observed as the mirror moves from one endpoint through the white-light null to the other endpoint modulates sky signals on time scales from 4 ms to 3 s. True sky signals are independent of the sign (near vs far side of null) and direction (forward vs back) of the mirror motion, allowing clean separation of sky signal from instrumental effects (detector time constant, responsivity). Sky rotation adds a third level of signal modulation. Unlike simple polarization-sensitive detectors, where instrument rotation produces a sinusoidal response to polarized sky signals, rotating the PIXIE instrument produces amplitude modulation of the *entire fringe pattern* at twice the spin frequency (Fig 13). The resulting modulated fringe pattern is readily distinguished from a simple spin-locked sine wave or its harmonics, suppressing potential spin-synchronous drifts.

Discrete instrument symmetries add a final layer of protection to identify and subtract potential systematic effects. The interference fringe pattern observed on each detector is symmetric with respect to zero phase delay, forcing any sky signal into the real part of the Fourier transform. The imaginary part of the Fourier transform provides a clean test for systematics as well as an independent realization of the noise. Note that since the real and imaginary parts of the Fourier transform are both derived from the same full data set, the real–imaginary comparison tests systematics at the full mission sensitivity without the usual $\sqrt{2}$ reduction for jack knife tests requiring separate halves of the data.

PIXIE employs a number of discrete symmetries, each of which relates to a different combination of instrumental effects. A partial list includes

- A-side beam vs B-side beam
- Left-side vs right-side detectors
- Horizontal vs vertical polarization
- Forward vs backward motion of the MTM phase-delay mechanism
- Calibrator on A-side beam vs B-side beam
- Instrument hotter vs colder than sky
- Observations on ascending vs descending node on sky

Figure 14 summarizes PIXIE's ability to suppress, identify, and subtract potential systematic errors. The combined systematic error budget is an order of magnitude fainter than either the B-mode signal at $r = 0.01$ or a spectral distortion at $|y| = 10^{-8}$. Recall that PIXIE is a spectrometer: the spectral dependence of instrumental effects differs from expected sky signals, further reducing the impact for astrophysical observations. For a more detailed description of PIXIE's systematic error suppression, see the discussion in 35.

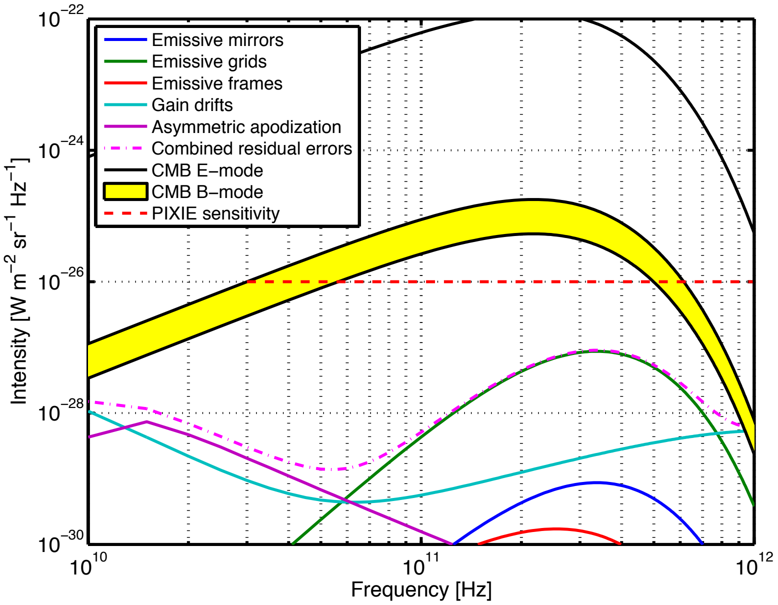

Figure 14. Frequency spectra of residual systematic errors compared to CMB E-mode (solid black line) and B-mode at $0.01 < r < 0.1$ (yellow band). The dashed red line shows the instrument noise level. Systematic errors do not contribute appreciably to the combined noise budget.

4. FOREGROUNDS

We view the CMB through a screen of diffuse Galactic emission originating within different components of the interstellar medium. Figure 15 compares the predicted B-mode signal to polarized Galactic foregrounds. Synchrotron emission from relativistic cosmic ray electrons accelerated in the Galactic magnetic field dominates the diffuse radio continuum at low frequencies. The frequency spectrum of synchrotron radiation depends on the cosmic ray energy spectrum. For a power-law distribution of cosmic ray energy $N(E) \sim E^{-p}$, the synchrotron intensity is also a power law,

$$I_s(\nu) = A_s \left(\frac{\nu}{\nu_s} \right)^{\beta_s}, \tag{18}$$

where ν is the observing frequency and $\beta_s = (1-p)/2$ is defined relative to reference frequency $\nu_s \sim 0.3$ GHz. The measured values $2.6 < p < 3.2$ for the cosmic ray energy spectrum correspond to synchrotron spectral index $-1.1 < \beta_s < -0.8$, in reasonable agreement with radio data.[36–38] Synchrotron emission is intrinsically polarized, with fractional polarization $f_s = (p+1)/(p+7/3) \sim 0.7$ oriented perpendicular to the local magnetic field. Beam smearing and line of sight effects average over multiple regions with different field alignment, so that the observed polarization is typically much lower.[1,39]

Dust is the dominant foreground at high frequencies. Dust grains in the interstellar medium absorb optical and UV photons and re-radiate the energy in the far-infrared. The resulting spectrum is often empirically modeled as a modified blackbody

$$I_d(\nu) = \epsilon B_\nu(T) \left(\frac{\nu}{\nu_d} \right)^{\beta_d} \tag{19}$$

where $B_\nu(T)$ is the Planck intensity at temperature T, and the emissivity ϵ and spectral index β_d are defined at reference frequency $\nu_d \sim 3$ THz. Irregular grains tend to align in the Galactic magnetic field; the higher radiation efficiency along the long axis results in dust emission polarized (like synchrotron emission) perpendicular to the magnetic field. The observed polarization fraction is as high as 0.2 for high-latitude lines of sight.[40]

Additional foregrounds contribute to the total intensity, but are largely unpolarized. Free-free emission from the ionized interstellar medium follows a power-law spectrum $I_{\rm ff} {\sim} \nu^{\beta_{\rm ff}}$ with spectral index $\beta_{\rm ff} \approx -0.14$.[41] A growing body of evidence suggests that a substantial fraction of the diffuse continuum near 20 GHz consists of electric dipole radiation from a population of small, rapidly spinning dust grains.[42,43] Spinning dust emission is expected to peak at frequencies near 20 GHz. Both the free-free and spinning dust foregrounds are significant only at frequencies below 100 GHz, and are unimportant compared to the dominant dust emission at higher frequencies.

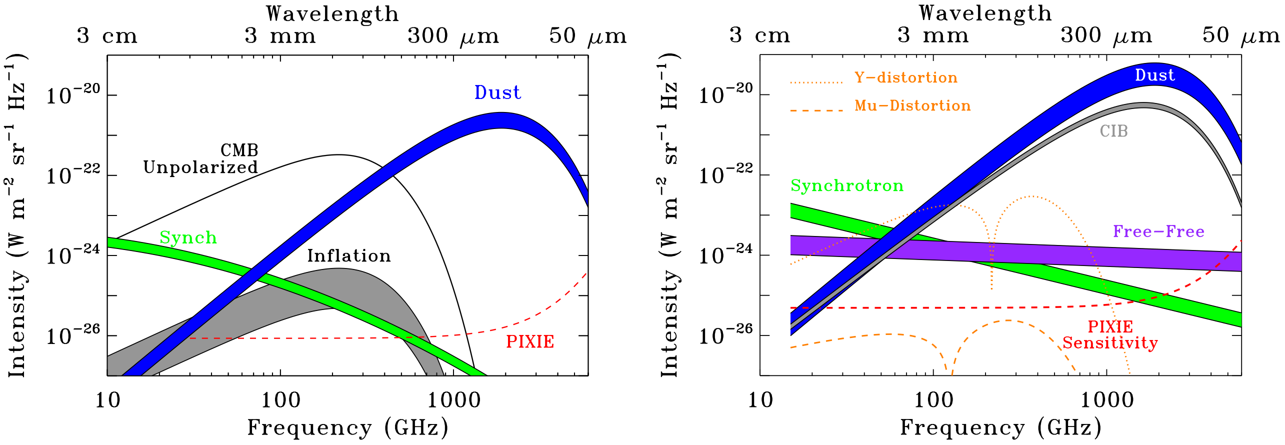

Figure 15. Foregrounds vs cosmic signals for polarized (left) and unpolarized (right) sources. Separating the cosmic signals requires subtracting foregrounds to sub-percent accuracy.

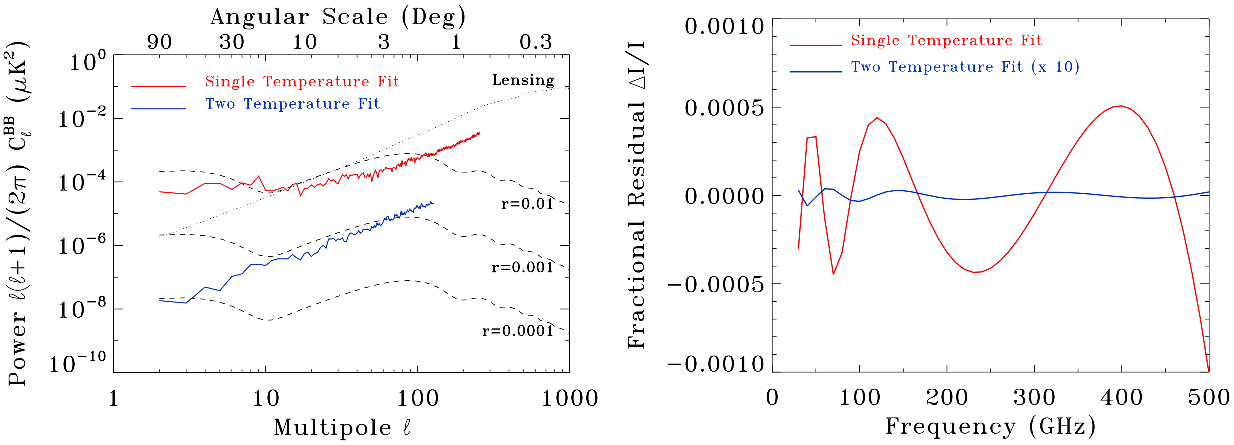

Figure 16. CMB residuals after fitting modified-blackbody dust models to simulations generated from transient-heating dust models. (Left) B-mode power spectrum of fitted CMB component. (Right) Fractional residual $\Delta I/I$ for (CMB + foreground) for a median sky pixel. Incorrect dust parameterization fits the combined sky emission to precision $\Delta I/I < 2 \times 10^{-6}$ but yields a false CMB detection at level $\Delta r > 0.001$.

Foregrounds are brighter than the expected cosmological signals for both polarization and spectral distortions. Recovering the cosmic signal requires removing foregrounds to sub-percent accuracy. PIXIE's combination of broad frequency coverage with excellent absolute band-to-band calibration provides a unique data set to identify and model far-IR foregrounds.

A key concern is the dust foreground. Dust is the dominant foreground at frequencies above 70 GHz, including the peak of the CMB intensity. Unlike the low-frequency synchrotron and free-free components, whose spectral dependence is constrained by observations of the cosmic-ray and thermal electron distributions, the frequency spectrum of far-IR dust emission must be determined by direct measurement. Dust is commonly modeled as a modified blackbody (Eq. 19), with one or two discrete temperature components. This can at best only approximate the true dust distribution. The dust emission spectrum represents a balance between optical/UV power absorbed by each grain and subsequently re-radiated in the far-infrared. It thus depends on both the absorption and emission properties of individual dust grains as well as the stellar radiation field illuminating each grain. All of these will vary within the interstellar medium. The stellar radiation field *must* vary as individual dust grains lie at different distances from individual stellar sources. Differences in the physical properties of dust grains yield additional temperature differences, with carbonaceous grains systematically colder than silicates.[44–51] Differences in grain size drive further temperature variation. Transient heating of small grains also causes temperature variation, even within a homogeneous dust population illuminated by a uniform stellar radiation field.

More realistic distributions of dust temperature will create significant biases in the fitted CMB and foreground parameters unless the fitted model adequately captures the underlying dust spectrum. We illustrate this with simple toy models. One alternative retains two temperature peaks, but broadens the distribution using a Gaussian smoothing to include emission at intermediate temperatures as well. We additionally consider a model with a single peak at low temperature T_0 plus an extended "tail" to higher temperatures

$$\epsilon(T) = \epsilon(T_0) \left(\frac{T}{T_0} \right)^{\kappa} \tag{20}$$

to approximate the effect of transient heating. For both models, we adjust the relative amplitudes of the warm and cold components so that emission from the cold component remains at the observed 3.7% of the power from the warm component, while normalizing the combined dust emission to match the intensity of Planck polarized dust model at 353 GHz. We evaluate the resulting toy models in Stokes Q and U for 30 noiseless frequency channels from 30 to 500 GHz, and add synchrotron emission to each pixel following the Planck polarized synchrotron model. We then fit the combined foreground emission in each pixel outside the Planck HFI polarization mask to superposition of CMB, synchrotron, and dust emission, where the fitted model (incorrectly) assumes the one- or two-component modified blackbody parameterization for the dust. Figure 16 shows the resulting B-mode power spectrum for the fitted CMB component. The commonly-used modified-blackbody models produce non-trivial bias. Fitting the transient-heating input with a single temperature component yields bias $\Delta r \sim 0.01$ with precision $\Delta I/I < 5 \times 10^{-4}$. Even the two-component fit shows bias bias $\Delta r \sim 0.001$ despite achieving precision $\Delta I/I < 2 \times 10^{-6}$.

Figure 16 demonstrates the importance of using the correct functional form for the far-IR dust emission: fitting different dust models to the same input sky can produce different CMB results despite reproducing the combined sky emission to high precision.

Foreground models must be accurate as well as precise. Data at THz frequencies is critical for distinguishing dust models: PIXIE observes dust at signal to noise ratio > 1000 for each pixel and each frequency bin at THz frequencies where dust emission peaks. Models that are nearly degenerate at millimeter wavelengths where the CMB is brightest are readily distinguished at THz frequencies where color temperature differences dominate the spectra.

5. SUMMARY

PIXIE will map the full sky in absolute intensity and linear polarization (Stokes I, Q, and U) with angular resolution $2.^{\circ}6$ in each of 400 frequency channels 14.8 GHz wide from 30 GHz to 6 THz. The calibrated spectral data at each frequency will be binned into 49152 sky pixels each $0.^{\circ}9$ in diameter using the HEALPIX pixelization.[52] Typical sensitivities within each mid-latitude pixel are

$$\delta I_\nu^I = 4 \times 10^{-24} \text{ W m}^{-2} \text{ s}^{-1} \text{ sr}^{-1}$$

for Stokes I and

$$\delta I_\nu^{QU} = 6 \times 10^{-25} \text{ W m}^{-2} \text{ s}^{-1} \text{ sr}^{-1}$$

for Stokes Q or U. The resulting data set supports a broad range of science goals.

- **CMB Polarization:** PIXIE will map CMB polarization to sensitivity 70 nK per 1° × 1° pixel. PIXIE will map the gravitational signature of inflation at sensitivity $\delta r = 2 \times 10^{-4}$, providing a critical test for large-field inflation models. PIXIE will characterize the optical depth of the universe to produce a 3σ detection of the neutrino mass.
- **Spectral Distortions:** PIXIE will compare the sky to a full-aperture calibrator to map deviations from a blackbody spectrum. PIXIE will improve the FIRAS limits by three orders of magnitude, reaching limits $|\mu| < 10^{-8}$ for a chemical potential distortion and $|y| < 2 \times 10^{-9}$ for a Compton distortion. Measurements at these sensitivities probe a variety of physical processes in the early universe, including dissipation of primordial density perturbations, decay or annihilation of dark matter, the physics of recombination, and the growth of structure in the universe.
- **Interstellar Medium:** PIXIE's all-sky spectral cubes provide important insights into the interstellar medium (ISM) within the Galaxy. In addition, PIXIE will map far-IR line emission from both molecular and atomic species to characterize the temperature, density, and radiation fields within distinct phases of the interstellar medium The well-calibrated PIXIE data spanning 7 octaves in frequency will be a legacy data set for astrophysics, providing inputs for detailed models of the interstellar medium as well as precision calibration sources for future far-IR missions.

PIXIE's primary goals are to characterize primordial inflation through the signature in CMB polarization, and to constrain energetic processes in the early universe through measurements of spectral distortions. These goals reflect priorities outlined in the 2010 *New Worlds, New Horizons* Astrophysics Decadal Survey and further endorsed by NASA's Astrophysics Roadmap *Enduring Quests, Daring Visions*.[53] PIXIE is technologically mature and can achieve these goals within the resources of the existing Explorer program.

REFERENCES

[1] Planck Collaboration, Ade, P. A. R., Aghanim, N., Arnaud, M., Ashdown, M., Aumont, J., Baccigalupi, C., Banday, A. J., Barreiro, R. B., Bartlett, J. G., and et al., "Planck 2015 results. XIII. Cosmological parameters," *ArXiv e-prints* (Feb. 2015).

[2] Rubakov, V. A., Sazhin, M. V., and Veryaskin, A. V., "Graviton creation in the inflationary universe and the grand unification scale," *Physics Letters B* **115**, 189–192 (Sept. 1982).

[3] Fabbri, R. and Pollock, M. D., "The effect of primordially produced gravitons upon the anisotropy of the cosmological microwave background radiation," *Physics Letters B* **125**, 445–448 (June 1983).

[4] Abbott, L. F. and Wise, M. B., "Constraints on generalized inflationary cosmologies," *Nuclear Physics B* **244**, 541–548 (Oct. 1984).

[5] Polnarev, A. G., "Polarization and anisotropy induced in the microwave background by cosmological gravitational waves," *Astronomicheskii Zhurnal* **62**, 1041–1052 (Dec. 1985).

[6] Davis, R. L., Hodges, H. M., Smoot, G. F., Steinhardt, P. J., and Turner, M. S., "Cosmic microwave background probes models of inflation," *Physical Review Letters* **69**, 1856–1859 (Sept. 1992).

[7] Grishchuk, L. P., "Cosmological perturbations of quantum-mechanical origin and anisotropy of the microwave background," *Physical Review Letters* **70**, 2371–2374 (Apr. 1993).

[8] Kamionkowski, M., Kosowsky, A., and Stebbins, A., "Statistics of cosmic microwave background polarization," *Physical Review D* **55**, 7368–7388 (June 1997).

[9] Seljak, U. and Zaldarriaga, M., "Signature of Gravity Waves in the Polarization of the Microwave Background," *Physical Review Letters* **78**, 2054–2057 (Mar. 1997).

[10] Zeldovich, Y. B. and Sunyaev, R. A., "The Interaction of Matter and Radiation in a Hot-Model Universe," *Astrophysics and Space Science* **4**, 301–316 (July 1969).

[11] Sunyaev, R. A. and Zeldovich, I. B., "Microwave background radiation as a probe of the contemporary structure and history of the universe," *Ann Rev of Astronomy and Astrophysics* **18**, 537–560 (1980).

[12] Danese, L. and de Zotti, G., "Double Compton process and the spectrum of the microwave background," *Astronomy and Astrophysics* **107**, 39–42 (Mar. 1982).

[13] Bartlett, J. G. and Stebbins, A., "Did the universe recombine?," *The Astrophysical Journal* **371**, 8–13 (Apr. 1991).

[14] Chluba, J. and Sunyaev, R. A., "The evolution of CMB spectral distortions in the early Universe," *Monthly Notices of the Royal Astronomical Society* **419**, 1294–1314 (Jan. 2012).

[15] Kogut, A., Fixsen, D. J., Chuss, D. T., Dotson, J., Dwek, E., Halpern, M., Hinshaw, G. F., Meyer, S. M., Moseley, S. H., Seiffert, M. D., Spergel, D. N., and Wollack, E. J., "The Primordial Inflation Explorer (PIXIE): a nulling polarimeter for cosmic microwave background observations," *Journal of Cosmology and Astroparticle Physics* **7**, 25 (July 2011).

[16] Keisler, R., Hoover, S., Harrington, N., Henning, J. W., Ade, P. A. R., Aird, K. A., Austermann, J. E., Beall, J. A., Bender, A. N., Benson, B. A., Bleem, L. E., Carlstrom, J. E., Chang, C. L., Chiang, H. C., Cho, H.-M., Citron, R., Crawford, T. M., Crites, A. T., de Haan, T., Dobbs, M. A., Everett, W., Gallicchio, J., Gao, J., George, E. M., Gilbert, A., Halverson, N. W., Hanson, D., Hilton, G. C., Holder, G. P., Holzapfel, W. L., Hou, Z., Hrubes, J. D., Huang, N., Hubmayr, J., Irwin, K. D., Knox, L., Lee, A. T., Leitch, E. M., Li, D., Luong-Van, D., Marrone, D. P., McMahon, J. J., Mehl, J., Meyer, S. S., Mocanu, L., Natoli, T., Nibarger, J. P., Novosad, V., Padin, S., Pryke, C., Reichardt, C. L., Ruhl, J. E., Saliwanchik, B. R., Sayre, J. T., Schaffer, K. K., Shirokoff, E., Smecher, G., Stark, A. A., Story, K. T., Tucker, C., Vanderlinde, K., Vieira, J. D., Wang, G., Whitehorn, N., Yefremenko, V., and Zahn, O., "Measurements of Sub-degree B-mode Polarization in the Cosmic Microwave Background from 100 Square Degrees of SPTpol Data," *The Astrophysical Journal* **807**, 151 (July 2015).

[17] The Polarbear Collaboration: P. A. R. Ade, Akiba, Y., Anthony, A. E., Arnold, K., Atlas, M., Barron, D., Boettger, D., Borrill, J., Chapman, S., Chinone, Y., Dobbs, M., Elleflot, T., Errard, J., Fabbian, G., Feng, C., Flanigan, D., Gilbert, A., Grainger, W., Halverson, N. W., Hasegawa, M., Hattori, K., Hazumi, M., Holzapfel, W. L., Hori, Y., Howard, J., Hyland, P., Inoue, Y., Jaehnig, G. C., Jaffe, A. H., Keating, B., Kermish, Z., Keskitalo, R., Kisner, T., Le Jeune, M., Lee, A. T., Leitch, E. M., Linder, E., Lungu, M., Matsuda, F., Matsumura, T., Meng, X., Miller, N. J., Morii, H., Moyerman, S., Myers,

M. J., Navaroli, M., Nishino, H., Orlando, A., Paar, H., Peloton, J., Poletti, D., Quealy, E., Rebeiz, G., Reichardt, C. L., Richards, P. L., Ross, C., Schanning, I., Schenck, D. E., Sherwin, B. D., Shimizu, A., Shimmin, C., Shimon, M., Siritanasak, P., Smecher, G., Spieler, H., Stebor, N., Steinbach, B., Stompor, R., Suzuki, A., Takakura, S., Tomaru, T., Wilson, B., Yadav, A., and Zahn, O., "A Measurement of the Cosmic Microwave Background B-mode Polarization Power Spectrum at Sub-degree Scales with POLARBEAR," *The Astrophysical Journal* **794**, 171 (Oct. 2014).

[18] BICEP2 Collaboration, Keck Array Collaboration, Ade, P. A. R., Ahmed, Z., Aikin, R. W., Alexander, K. D., Barkats, D., Benton, S. J., Bischoff, C. A., Bock, J. J., Bowens-Rubin, R., Brevik, J. A., Buder, I., Bullock, E., Buza, V., Connors, J., Crill, B. P., Duband, L., Dvorkin, C., Filippini, J. P., Fliescher, S., Grayson, J., Halpern, M., Harrison, S., Hilton, G. C., Hui, H., Irwin, K. D., Karkare, K. S., Karpel, E., Kaufman, J. P., Keating, B. G., Kefeli, S., Kernasovskiy, S. A., Kovac, J. M., Kuo, C. L., Leitch, E. M., Lueker, M., Megerian, K. G., Netterfield, C. B., Nguyen, H. T., O'Brient, R., Ogburn, R. W., Orlando, A., Pryke, C., Richter, S., Schwarz, R., Sheehy, C. D., Staniszewski, Z. K., Steinbach, B., Sudiwala, R. V., Teply, G. P., Thompson, K. L., Tolan, J. E., Tucker, C., Turner, A. D., Vieregg, A. G., Weber, A. C., Wiebe, D. V., Willmert, J., Wong, C. L., Wu, W. L. K., and Yoon, K. W., "Improved Constraints on Cosmology and Foregrounds from BICEP2 and Keck Array Cosmic Microwave Background Data with Inclusion of 95 GHz Band," *Physical Review Letters* **116**, 031302 (Jan. 2016).

[19] Illarionov, A. F. and Siuniaev, R. A., "Comptonization, the spectrum of RELICT radiation, and the thermal history of the universe," *Astronomicheskii Zhurnal* **51**, 1162–1176 (Dec. 1974).

[20] Burigana, C., Danese, L., and de Zotti, G., "Formation and evolution of early distortions of the microwave background spectrum - A numerical study," *Astronomy & Astrophysics* **246**, 49–58 (June 1991).

[21] Chluba, J. and Jeong, D., "Teasing bits of information out of the CMB energy spectrum," *Monthly Notices of the Royal Astronomical Society* **438**, 2065–2082 (Mar. 2014).

[22] Fixsen, D. J., Cheng, E. S., Gales, J. M., Mather, J. C., Shafer, R. A., and Wright, E. L., "The Cosmic Microwave Background Spectrum from the Full COBE FIRAS Data Set," *The Astrophysical Journal* **473**, 576 (Dec. 1996).

[23] Planck Collaboration, Aghanim, N., Arnaud, M., Ashdown, M., Aumont, J., Baccigalupi, C., Banday, A. J., Barreiro, R. B., Bartlett, J. G., Bartolo, N., and et al., "Planck 2015 results. XXII. A map of the thermal Sunyaev-Zeldovich effect," *ArXiv e-prints* (Feb. 2015).

[24] Khatri, R. and Sunyaev, R., "Limits on the fluctuating part of y-type distortion monopole from Planck and SPT results," *Journal of Cosmology and Astroparticle Physics* **8**, 013 (Aug. 2015).

[25] Hill, J. C., Battaglia, N., Chluba, J., Ferraro, S., Schaan, E., and Spergel, D. N., "Taking the Universe's Temperature with Spectral Distortions of the Cosmic Microwave Background," *Physical Review Letters* **115**, 261301 (Dec. 2015).

[26] Daly, R. A., "Spectral distortions of the microwave background radiation resulting from the damping of pressure waves," *The Astrophysical Journal* **371**, 14–28 (Apr. 1991).

[27] Hu, W., Scott, D., and Silk, J., "Power spectrum constraints from spectral distortions in the cosmic microwave background," *The Astrophysical Journall* **430**, L5–L8 (July 1994).

[28] Chluba, J., Khatri, R., and Sunyaev, R. A., "CMB at 2 x 2 order: the dissipation of primordial acoustic waves and the observable part of the associated energy release," *Monthly Notices of the Royal Astronomical Society* **425**, 1129–1169 (Sept. 2012).

[29] Sunyaev, R. A. and Khatri, R., "Unavoidable CMB Spectral Features and Blackbody Photosphere of Our Universe," *International Journal of Modern Physics D* **22**, 1330014 (June 2013).

[30] McDonald, P., Scherrer, R. J., and Walker, T. P., "Cosmic microwave background constraint on residual annihilations of relic particles," *Physical Review D* **63**, 023001 (Jan. 2001).

[31] Kogut, A., Fixsen, D. J., and Hill, R. S., "Polarization properties of a broadband multi-moded concentrator," *Journal of the Optical Society of America A* **32**, 1040 (June 2015).

[32] Wollack, E. J., Fixsen, D. J., Henry, R., Kogut, A., Limon, M., and Mirel, P., "Electromagnetic and Thermal Properties of a Conductively Loaded Epoxy," *International Journal of Infrared and Millimeter Waves* **29**, 51–61 (Jan. 2008).

[33] Fixsen, D. J., Wollack, E. J., Kogut, A., Limon, M., Mirel, P., Singal, J., and Fixsen, S. M., "Compact radiometric microwave calibrator," *Review of Scientific Instruments* **77**, 064905 (June 2006).

[34] Mather, J. C., "Bolometer noise: nonequilibrium thoery," *Applied Optics* **21**, 1125–1129 (Mar. 1982).

[35] Nagler, P. C., Fixsen, D. J., Kogut, A., and Tucker, G. S., "Systematic Effects in Polarizing Fourier Transform Spectrometers for Cosmic Microwave Background Observations," *The Astrophysical Journal Supplement Series* **221**, 21 (Nov. 2015).

[36] Strong, A. W., Moskalenko, I. V., and Ptuskin, V. S., "Cosmic-Ray Propagation and Interactions in the Galaxy," *Annual Review of Nuclear and Particle Science* **57**, 285–327 (Nov. 2007).

[37] Jaffe, T. R., Banday, A. J., Leahy, J. P., Leach, S., and Strong, A. W., "Connecting synchrotron, cosmic rays and magnetic fields in the plane of the Galaxy," *Monthly Notices of the Royal Astronomical Society* **416**, 1152–1162 (Sept. 2011).

[38] Kogut, A., "Synchrotron Spectral Curvature from 22 MHz to 23 GHz," *The Astrophysical Journal* **753**, 110 (July 2012).

[39] Gold, B., Odegard, N., Weiland, J. L., Hill, R. S., Kogut, A., Bennett, C. L., Hinshaw, G., Chen, X., Dunkley, J., Halpern, M., Jarosik, N., Komatsu, E., Larson, D., Limon, M., Meyer, S. S., Nolta, M. R., Page, L., Smith, K. M., Spergel, D. N., Tucker, G. S., Wollack, E., and Wright, E. L., "Seven-year Wilkinson Microwave Anisotropy Probe (WMAP) Observations: Galactic Foreground Emission," *The Astrophysical Journal Supplement Series* **192**, 15 (Feb. 2011).

[40] Planck Collaboration, Ade, P. A. R., Aghanim, N., Alina, D., Alves, M. I. R., Armitage-Caplan, C., Arnaud, M., Arzoumanian, D., Ashdown, M., Atrio-Barandela, F., and et al., "Planck intermediate results. XIX. An overview of the polarized thermal emission from Galactic dust," *Astronomy and Atstrophysics* **576**, A104 (Apr. 2015).

[41] Bennett, C. L., Smoot, G. F., Hinshaw, G., Wright, E. L., Kogut, A., de Amici, G., Meyer, S. S., Weiss, R., Wilkinson, D. T., Gulkis, S., Janssen, M., Boggess, N. W., Cheng, E. S., Hauser, M. G., Kelsall, T., Mather, J. C., Moseley, Jr., S. H., Murdock, T. L., and Silverberg, R. F., "Preliminary separation of galactic and cosmic microwave emission for the COBE Differential Microwave Radiometer," *The Astrophysical Journal Letters* **396**, L7–L12 (Sept. 1992).

[42] Kogut, A., Banday, A. J., Bennett, C. L., Gorski, K. M., Hinshaw, G., and Reach, W. T., "High-Latitude Galactic Emission in the COBE Differential Microwave Radiometer 2 Year Sky Maps," *The Astrophsyical Journal* **460**, 1 (Mar. 1996).

[43] Planck Collaboration, Ade, P. A. R., Aghanim, N., Arnaud, M., Ashdown, M., Aumont, J., Baccigalupi, C., Balbi, A., Banday, A. J., Barreiro, R. B., and et al., "Planck early results. XX. New light on anomalous microwave emission from spinning dust grains," *Astronomy and Astrophysics* **536**, A20 (Dec. 2011).

[44] Gezari, D. Y., Joyce, R. R., and Simon, M., "Observations of the Galactic Nucleus at 350 Microns," *The Astrophysical Journal Letters* **179**, L67 (Jan. 1973).

[45] Draine, B. T. and Lee, H. M., "Optical properties of interstellar graphite and silicate grains," *The Astrophysical Journal* **285**, 89–108 (Oct. 1984).

[46] Rowan-Robinson, M., "On the nature of interstellar grains and the interpretation of the IRAS background radiation," *Monthly Notices of the Royal Astronomical Society* **219**, 737–749 (Apr. 1986).

[47] Zubko, V., Dwek, E., and Arendt, R. G., "Interstellar Dust Models Consistent with Extinction, Emission, and Abundance Constraints," *The Astrophysical Journal Supplement Series* **152**, 211–249 (June 2004).

[48] Draine, B. T. and Li, A., "Infrared Emission from Interstellar Dust. IV. The Silicate-Graphite-PAH Model in the Post-Spitzer Era," *The Astrophysical Journal* **657**, 810–837 (Mar. 2007).

[49] Draine, B. T. and Fraisse, A. A., "Polarized Far-Infrared and Submillimeter Emission from Interstellar Dust," *The Astrophysical Journal* **696**, 1–11 (May 2009).

[50] Compiègne, M., Verstraete, L., Jones, A., Bernard, J.-P., Boulanger, F., Flagey, N., Le Bourlot, J., Paradis, D., and Ysard, N., "The global dust SED: tracing the nature and evolution of dust with DustEM," *Astronomy and Astrophysics* **525**, A103 (Jan. 2011).

[51] Jones, A. P., Fanciullo, L., Köhler, M., Verstraete, L., Guillet, V., Bocchio, M., and Ysard, N., "The evolution of amorphous hydrocarbons in the ISM: dust modelling from a new vantage point," *Astronomy and Astrophysics* **558**, A62 (Oct. 2013).

[52] Górski, K. M., Hivon, E., Banday, A. J., Wandelt, B. D., Hansen, F. K., Reinecke, M., and Bartelmann, M., "HEALPix: A Framework for High-Resolution Discretization and Fast Analysis of Data Distributed on the Sphere," *The Astrophysical Journal* **622**, 759–771 (Apr. 2005).

[53] Kouveliotou, C., Agol, E., Batalha, N., Bean, J., Bentz, M., Cornish, N., Dressler, A., Figueroa-Feliciano, E., Gaudi, S., Guyon, O., Hartmann, D., Kalirai, J., Niemack, M., Ozel, F., Reynolds, C., Roberge, A., Straughn, K. S. A., Weinberg, D., and Zmuidzinas, J., "Enduring Quests-Daring Visions (NASA Astrophysics in the Next Three Decades)," *ArXiv e-prints* (Jan. 2014).